A method for estimating the ring current structure and the electric potential distribution using energetic neutral atom data assimilation

S. Nakano,[1,2] G. Ueno,[1,2] Y. Ebihara,[3] M.-C. Fok,[4] S. Ohtani,[5] P. C. Brandt,[5] D. G. Mitchell,[5] K. Keika,[6] and T. Higuchi[1,2]

Received 15 May 2006; revised 3 December 2007; accepted 11 February 2008; published 10 May 2008.

[1] We present a technique for estimating ring current ion distributions and electric potential in the inner magnetosphere by incorporating data from the High-Energy Neutral Atom (HENA) imager on the IMAGE satellite into a kinetic ring current model in the context of data assimilation. Data assimilation is an approach which adjusts a physics-based model according to differences with observations. We perform the data assimilation using the particle filter (PF) which is applicable to high-dimensional systems and observations with relatively low computational cost. In the present technique, the magnetospheric electric potential distribution is represented by the sum of a Volland-Stern field and a deviation, and the deviation is improved in the assimilation process. The ring current ion distribution is then determined from the electric potential distribution. The method is tested by assimilating artificial data generated by another simulation. The results demonstrate that the ring current ion distribution is successfully reconstructed by the proposed algorithm and that the distorted structures of the electric potential distribution are also well reproduced. An example to illustrate how the present technique could be applied for assimilating a real IMAGE/HENA data set is also demonstrated. This technique provides a useful tool for investigating the global dynamic structure of ring current and electric potential.

Citation: Nakano, S., G. Ueno, Y. Ebihara, M.-C. Fok, S. Ohtani, P. C. Brandt, D. G. Mitchell, K. Keika, and T. Higuchi (2008), A method for estimating the ring current structure and the electric potential distribution using energetic neutral atom data assimilation, *J. Geophys. Res.*, *113*, A05208, doi:10.1029/2006JA011853.

1. Introduction

[2] The magnetospheric ring current during magnetic storms has been simulated by many approaches, providing a wide variety of qualitative overviews of its development and decay [e.g., *Chen et al.*, 1993; *Ebihara and Ejiri*, 2000; *Fok et al.*, 1995, 2001; *Jordanova et al.*, 1996]. However, as knowledge on the inner magnetosphere remains limited, such models contain many uncertain assumptions. For example, owing to the sparsity of available data on electric fields in the magnetosphere, most ring current simulations utilize an electric potential distribution model such as the Volland-Stern model [e.g., *Ebihara and Ejiri*, 2000; *Fok et al.*, 1995], the model by *McIlwain* [1986] [e.g., *Liemohn et al.*, 2001a], which are not guaranteed to be always accurate. In this way, inputs to simulation models of storm-time ring current contain inherent uncertainties in the structure of electric fields, the initial and boundary conditions, and so on, resulting in uncertainties or inaccuracies in the simulation output.

[3] One method to reduce the uncertainties or inaccuracies of the simulation is to incorporate observed data into a model, a procedure referred to as data assimilation. There have been several studies which used in situ plasma observations for improving magnetospheric models [e.g., *Kistler et al.*, 1989; *Liemohn et al.*, 2001]. Recent development of observation systems allows us to obtain more detailed information on the magnetosphere with better spatial coverage and temporal resolution, which offers the possibility to comprehensively reduce uncertainties in simulation models. In particular, the IMAGE satellite provides global imaging data for energetic neutral atoms (ENAs), which gives spatially wide-ranging information to improve a ring current model. In this paper, we propose a technique for modeling the temporal evolution of the ring current ion distribution by assimilating a time sequence of the data of the high-energy neutral atom (HENA) imager [*Mitchell et al.*, 2000] on board the IMAGE satellite.

[4] The present data assimilation technique is designed to apply to a simplified version of the comprehensive ring

[1]Institute of Statistical Mathematics, Research Organization of Information and Systems, Tokyo, Japan.
[2]Japan Science and Technology Agency, Saitama, Japan.
[3]Institute for Advanced Research, Nagoya University, Nagoya, Japan.
[4]NASA Goddard Space Flight Center, Greenbelt, Maryland, USA.
[5]Johns Hopkins University Applied Physics Laboratory, Laurel, Maryland, USA.
[6]Space Research Institute, Austrian Academy of Sciences, Graz, Austria.

Copyright 2008 by the American Geophysical Union.
0148-0227/08/2006JA011853

current model (CRCM) [*Fok et al.*, 2001] in which the electric field is expressed in a rather simple manner. By assimilating ENA data, initial settings of this ring current model are improved so as to be consistent to observations. While the IMAGE/HENA data can be used to deduce snapshots of the global distribution of ring current ions at each observation time independently [*Brandt et al.*, 2002b; *DeMajistre et al.*, 2004; *Vallat et al.*, 2004; *Perez et al.*, 2004], data assimilation allows static estimates of the ring current distribution from the IMAGE/HENA data to be evolved into a dynamic model that considers the physical consistencies described by this ring current model.

[5] In order to incorporate the IMAGE/HENA data into the simplified CRCM, one consideration is the high-dimensionality of the simulation model and the observation. The algorithms which were used in the past several attempts to assimilate observed data into magnetospheric simulation models do not work for the present ENA data assimilation. For example, several studies have directly inserted in situ particle flux data observed by geosynchronous satellites into simulation models of the inner magnetosphere [e.g., *Garner et al.*, 1999; *Liemohn et al.*, 2001]. However, direct insertion of a large number of data, which contain observational errors, might destroy continuity and physical consistency in the model. Moreover, such approaches are valid only when some of the variables in the simulation models can be measured or directly derived from measured data. Thus, these approaches cannot be used for the assimilation of ENA data, which reflect an integral of ion density along a line of sight and do not directly indicate the ion density at any point. *Naehr and Toffoletto* [2005] have proposed a method to assimilate in situ flux data into a simple radiation belt model using an extended Kalman filter. However, for models with high nonlinearity, the extended Kalman filter causes errors to diverge [e.g., *Evensen*, 1992]. In addition, when the system model for data assimilation contains a large number of variables, use of the extended Kalman filter is not realistic due to the prohibitive computational cost. The extended Kalman filter is thus impractical for data assimilation in the ring current model, which contains more than 2,000,000 variables. In meteorology and physical oceanography, some data assimilation algorithms which allow us to incorporate a high-dimensional observation into a high-dimensional model with relatively low computational cost are proposed and used for various applications. The particle filter (PF) algorithm [*Gordon et al.*, 1993; *Kitagawa*, 1993, 1996] (see *Kitagawa and Gersch* [1996] for details) is one of such algorithms. The proposed technique uses the PF to accomplish the data assimilation of the ENA data set. In the following, the data assimilation technique of the IMAGE/HENA data into the CRCM is introduced. In order to evaluate the technique, a data assimilation experiment is also performed using artificial data generated by another simulation run with a different electric field model.

2. Strategy of Assimilation

[6] The CRCM is a kinetic model that solves the bounce-averaged Boltzmann equation given by

$$\frac{\partial \bar{f}}{\partial t} + \langle \dot{l}_{is} \rangle \frac{\partial \bar{f}}{\partial l_{\mathrm{is}}} + \langle \dot{\phi}_{\mathrm{is}} \rangle \frac{\partial \bar{f}}{\partial \phi_{\mathrm{is}}} = -v\sigma\langle n \rangle \bar{f} - \left(\frac{\bar{f}}{0.5\tau_{\mathrm{b}}} \right)_{\mathrm{losscone}} \quad (1)$$

where $\bar{f}$ is the average phase-space density on the field line between the mirror points, l_{is} and ϕ_{is} indicate the magnetic latitude and longitude at the ionospheric altitude, σ is the cross section for charge exchange with neutrals, and n denotes the density of neutral atoms (see *Fok et al.* [2003] for details). In this study, only protons are considered. The CRCM, which provides the pitch angle distribution, allows us to predict the ENA flux observed by the HENA imager on board the IMAGE satellite [*Fok et al.*, 2003; *Ebihara and Fok*, 2004]. However, the predicted ENA flux could contain discrepancy with the observation due to errors or inaccuracies in assumptions underlying the model. The data assimilation reduces the discrepancy and provide a solution which is consistent with the observation.

[7] One of the critical factors controlling the global distribution of ring current ions is the electric field distribution in the inner magnetosphere, and accordingly the features of ENA images observed by the IMAGE satellite are also controlled by the electric field distribution [*Brandt et al.*, 2002a; *Fok et al.*, 2003]. Therefore, to accurately model the ring current distribution, it is important to obtain a realistic electric field distribution. However, there is no single established model for the electric field distribution in the inner magnetosphere, particularly during magnetic storms. It is thus presumed that the electrostatic potential distribution is uncertain, and the potential distribution is improved in the course of the data assimilation process. The approach for estimation of electric potential distribution in the present assimilation method is similar to that taken by *McIlwain* [1986] and *Kistler et al.* [1989], who also obtained information on the electric potential structure in the inner magnetosphere through the use of in situ ion spectra data and ion tracing. As electric potential distribution is estimated, the temporal evolution of the ring current ion distribution is determined in parallel.

[8] In the original CRCM by *Fok et al.* [2001], the electric potential distribution can be calculated by assuming self-consistency of the electric field and the electric current in the both magnetosphere and ionosphere on the basis of the Rice Convection Model (RCM). For simplicity, the ionospheric processes are not considered in the present assimilation method, although the result from a calculation of the electric potential distribution is used for a check of the assimilation scheme later. The magnetospheric electric field potential distribution at the equatorial plane is expressed as:

$$\Phi = \Phi_0 \left[\frac{r^2 \sin\phi}{R_0^2} + \sum_{\substack{0 \le i \le 3 \\ 1 \le j \le 3}} \mathcal{J}_i \left(\frac{\zeta_{ij} r}{R_0} \right) \left(a_{ij} \cos i\phi + b_{ij} \sin i\phi \right) \right] \quad (2)$$

where r is the radial distance from the Earth's center, ϕ is the magnetic local time in radians, R_0 is the equatorial radius of the outer boundary of the simulation domain, $\mathcal{J}_i$ is the ith order Bessel function, and ξ_{ij} are the positive roots of $\mathcal{J}_i(\xi_{ij}) = 0$ such that $0 < \xi_{i1} < \xi_{i2} < \cdots$. By assuming equipotentiality along a magnetic field line, electric potential at any point in the inner magnetosphere is given by that at the equatorial plane represented by equation (2). The parameter Φ_0 is set at the potential drop calculated from the model by *Weimer* [2001] with solar wind data obtained by the ACE as an input. The first term in the brackets on the

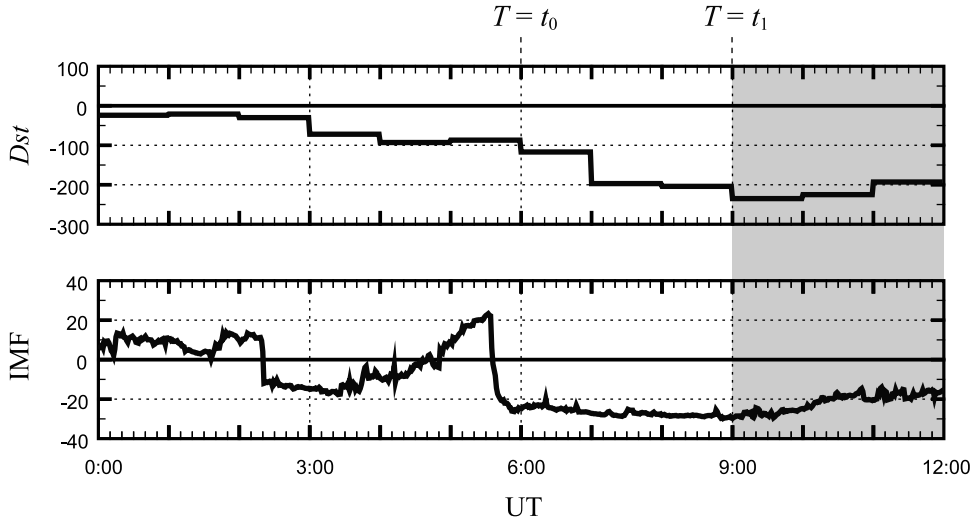

Figure 1. (top) D_{st} index for the period 0000–1200 UT, 12 August 2000. (bottom) Northward component of IMF in GSM coordinates, and B_z observed by the ACE spacecraft. IMF is plotted accounting for time delay from ACE to Earth (50 min). Model for assimilation is initialized at 0600 UT. HENA data are assumed to be available during the hatched period (0900 UT to 1200 UT).

right-hand side of equation (2) is the Volland-Stern-type electric field with a shielding factor of 2, and the deviation from the Volland-Stern-type electric field is represented by the second and third terms. At the outer boundary of the simulation domain, where $r = R_0$, the second and third terms become zero. The outer boundary condition of the electric potential is thus determined by the Volland-Stern-type electric field model. The coefficients a_{ij} and b_{ij} are uncertain, and optimal values of these coefficients are sought in order that the ENA flux estimated from the assimilation result fits the observed flux. The search for probable values of a_{ij} and b_{ij} is detailed in the appendix. For simplicity, it is assumed that a_{ij} and b_{ij} are constant over the simulated period. Therefore, temporal variations of the electric field are fully attributed to Φ_0. The ring current protons at the outer boundary are given by an isotropic Maxwellian with a temperature of 5 keV. The outer boundary of the simulation domain R_0 is set at $10R_E$. The proton density at the outer boundary is assumed to be unknown and an estimate of the proton density are obtained through data assimilation. The variation of the proton density at the outer boundary is assumed to follow a linear trend which is updated every hour. Conditions other than the magnetospheric electric potential and the ring current protons at the outer boundary are assumed to be given. The terrestrial magnetic main field is assumed to be a dipole field, and the magnetic fields due to magnetospheric currents are calculated by the models by *Tsyganenko* [1995] and *Tsyganenko and Stern* [1996] with the assumption that the tilt angle is zero.

[9] The differential flux of ENA J_{ENA} is obtained by a line-of-sight integral as

$$J_{\mathrm{ENA}} = \int (\sigma_{\mathrm{H}} n_{\mathrm{H}} + \sigma_{\mathrm{O}} n_{\mathrm{O}}) J_{\mathrm{proton}} \mathrm{d}s \tag{3}$$

where J_{proton} is the differential proton flux toward the IMAGE satellite and s is the distance along the line of sight. Assuming conservation of the first invariant, the proton differential flux J_{proton} at any point on the field line can be related to the equatorial differential flux, which can be readily derived from the phase-space density $\bar{f}$. The densities of neutral hydrogen and neutral oxygen are denoted by n_{H} and n_{O}, and σ_{H} and σ_{O} are the cross sections of charge exchange of ring current protons with neutral hydrogen and neutral oxygen. The neutral density distribution around the Earth is given by the model of *Rairden et al.* [1986] for hydrogen, and the neutral oxygen density distribution is given by the NRLMSISE-00 model [*Picone et al.*, 2002]. However, it is difficult to model the ENA flux properly from the optically thick region near the Earth. In the assimilation, ENA data containing ENA emissions near the Earth below and altitude of 1500 km are not included.

3. Evaluation With Artificial Data Set

3.1. Artificial Data for the Experiment

[10] The validity of the assimilation technique is evaluated by a data assimilation experiment using artificial ENA data generated by a different simulation run rather than real data obtained by the IMAGE satellite. As the result of assimilation of the artificial data can be checked by comparing with the simulation run which generated the artificial data, we can confirm whether the present scheme provides adequate estimations. The simulation for generation of artificial data is the same as that for the assimilation model except that the electric field distribution is calculated by the RCM as done by *Fok et al.* [2001] and that the proton density at the outer boundary is given by $N = 0.025N_{\mathrm{sw}} + 0.395$ (cm^{-3}) according to *Ebihara and Ejiri* [2000], where N_{sw} is the solar wind density. The position of the IMAGE satellite is assumed to be the same as the actual position. The HENA imager produces ENA images every 2 min covering an energy range of 10–200 keV. However, only ENA data for a single energy value (44.0 keV) at 12 min intervals are used in order to reduce the computational cost

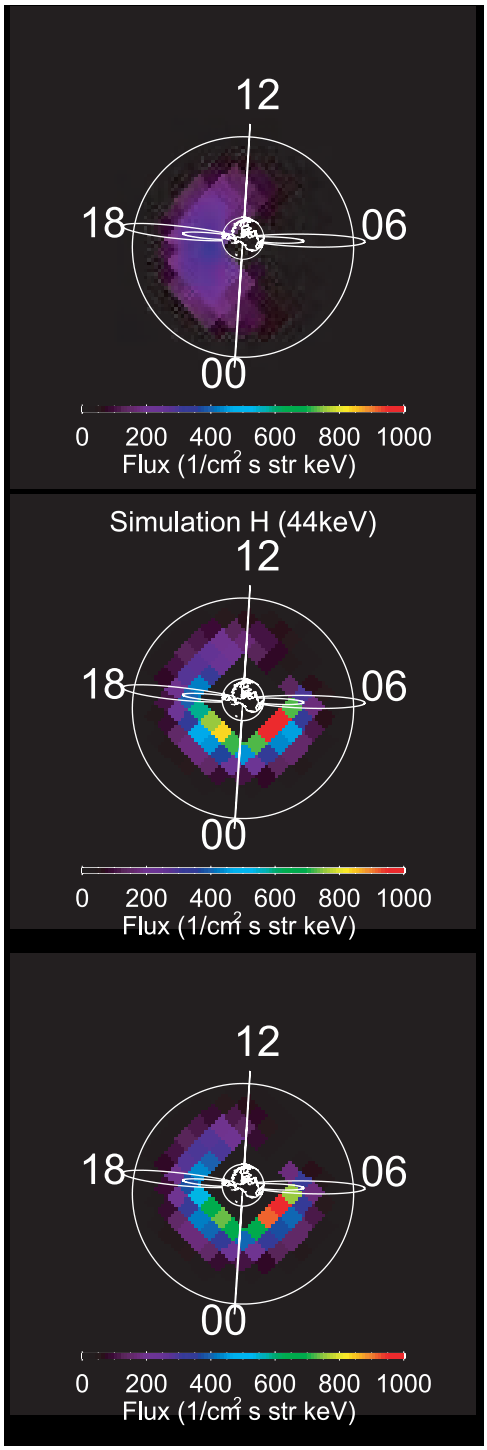

Figure 2. (top) Simulated ENA flux at 1000 UT assuming Volland-Stern model with a shielding factor of 2. (middle) ENA flux obtained by data assimilation of artificial HENA data. (bottom) Artificial HENA data.

here. The field of view of the HENA imager is 120°, and the angular resolution is 6° in elevation. The ENA data are obtained every 6° of spin. ENA data over a range of 120° centered at the earthward direction are used in the test, corresponding to a total of 20 × 20 data in each assimilation step. Considering that ENA count data contains Poisson

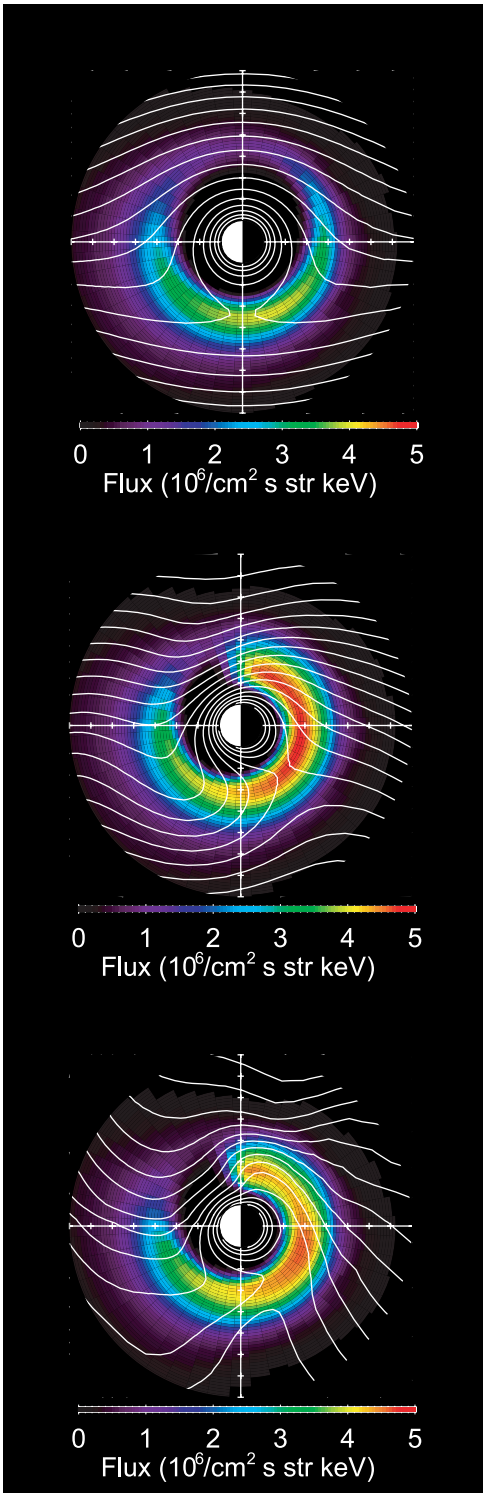

Figure 3. (top) Simulated proton flux distribution at 1000 UT assuming Volland-Stern model. (middle) Proton flux distribution obtained by data assimilation of artificial data. (bottom) Proton flux distribution in the model for generation of the artificial data. The contours of electric potential including the corotation electric field are also superimposed with contour interval 10 kV.

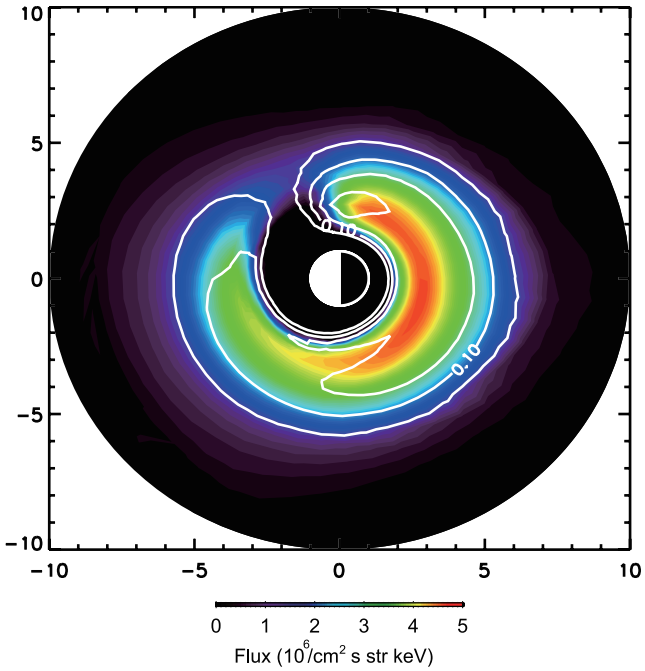

Figure 4. Uncertainty of the estimate of the ring current proton flux superimposed on the estimate of the flux which is also shown in the middle panel in Figure 3.

noises, an ENA datum for each pixel is artificially generated as follows. First, the ENA flux flowing into each pixel of the instrument is calculated from the run with the RCM. Second, the ENA flux is converted into an expectation of the detected ENA count during 1 spin for each pixel. Finally, assuming that an observed ENA count for each pixel obeys each Poisson distribution with the expectation, each count datum is generated by drawing from the distribution.

[11] The magnetic storm on 12 August 2000 was adopted for evaluation of the assimilation model. The disturbance field (D_{st}) index and the interplanetary magnetic field (IMF) observed by the ACE from 0000 UT to 1200 UT on this day are shown in Figure 1. The IMF B_z is plotted taking into account the time delay from the ACE to the Earth (assumed to be 50 min). The HENA data are assumed to be available during the period from 0900 UT to 1200 UT when the IMAGE satellite was near the apogee altitude (shaded period in Figure 1). The simulation run to generate the artificial data was started at 0200 UT, before the D_{st} index decreases. The initial distribution of ring current ions is given by the proton flux measured by AMPTE/CCE during quiescent times [*Sheldon and Hamilton*, 1993].

3.2. Result of the Experiment and Discussion

[12] The bottom panel of Figure 2 shows the reference ENA data at 1000 UT, which were artificially generated by the CRCM with the RCM, and the top panel shows the simulated ENA flux at 1000 UT assuming the Volland-Stern model of the magnetospheric electric field with a shielding factor of 2 (i.e., $a_{ij} = 0$ and $b_{ij} = 0$ for all i and j). The top panel represents the ENA flux estimated without data assimilation, because we can only assume that all the coefficients a_{ij} and b_{ij} are zero without using the information of the ENA observation. The two sets of results clearly differ in terms of both the intensity and the position of the peaks. The middle panel shows the ENA flux at 1000 UT derived from the results of data assimilation. The flux is improved markedly from that in the top panel. The peak of ENA emission in the postmidnight [*Brandt et al.*, 2002a; *Fok et al.*, 2003; *Ebihara and Fok*, 2004], which is not seen in the top panel, is also reproduced.

[13] Figure 3 shows the ring current proton distributions from which the ENA images shown in Figure 2 were generated. The ring current distributions are indicated in proton flux averaged over pitch angle at the equatorial

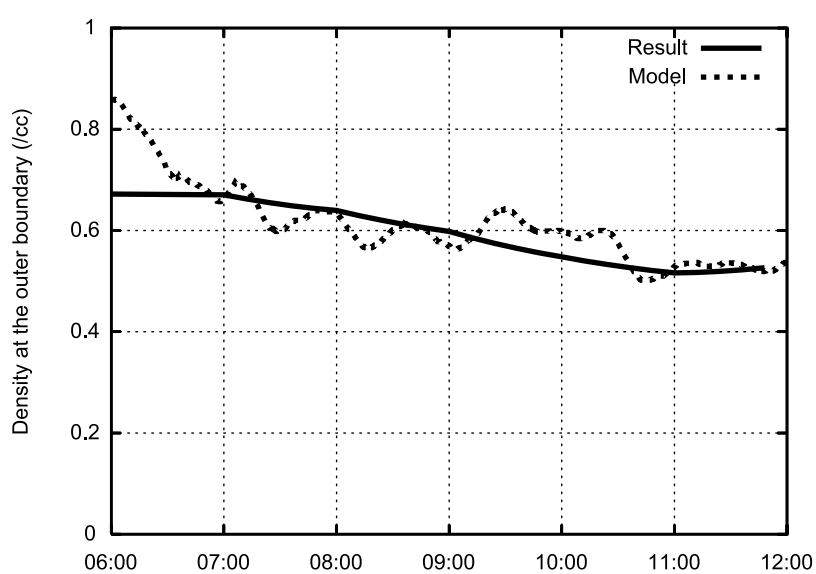

Figure 5. The proton density at the outer boundary of the simulation domain estimated using data assimilation of artificial data (solid line) and plasma sheet ion density given by the equation of *Ebihara and Ejiri* [2000], which was used in the reference simulation (dotted line).

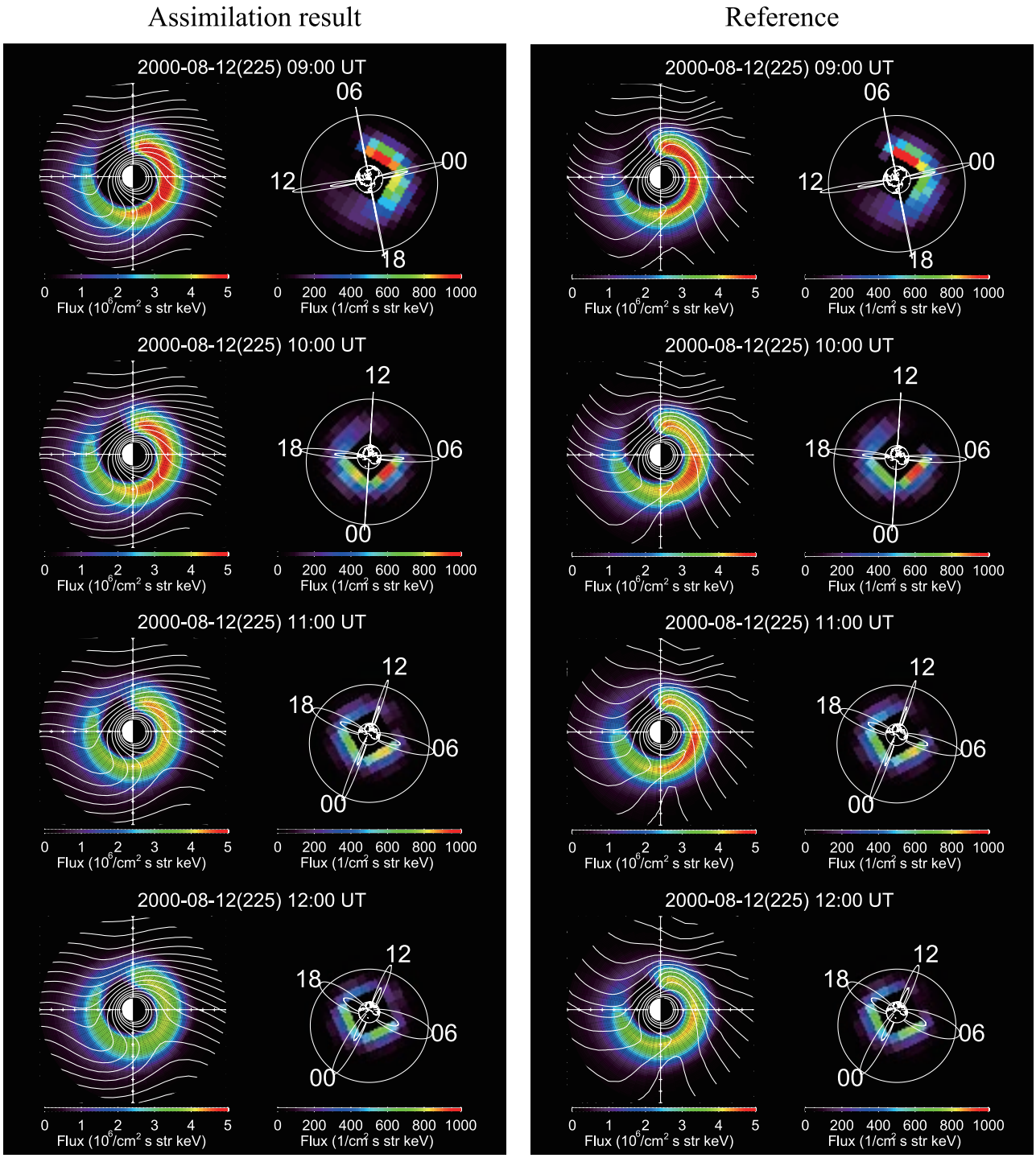

Figure 6. (left) Proton flux distribution obtained by data assimilation of artificial ENA data and ENA image derived from the result for every hour from 0900 UT to 1200 UT. (right) Proton flux distribution in the model for generation of the artificial data and the artificial ENA data for every hour from 0900 UT to 1200 UT.

plane. It is demonstrated that the ion distribution was successfully reproduced by the data assimilation. When the Volland-Stern type electric field is imposed in the magnetosphere, the ring current ion flux peaks around dusk and the ion flux becomes low in the postmidnight period. On the other hand, the assimilation result in the middle panel indicates that the ring current ion flux remains high throughout the night, consistent with the reference simulation model. Figure 4 shows uncertainty of the estimate of the ring current proton flux for reference. Here, the uncertainty is indicated by 2σ of the estimate which can be derived from the smoothed distribution (see Appendix A). Although the uncertainty is about 5% of the peak around the

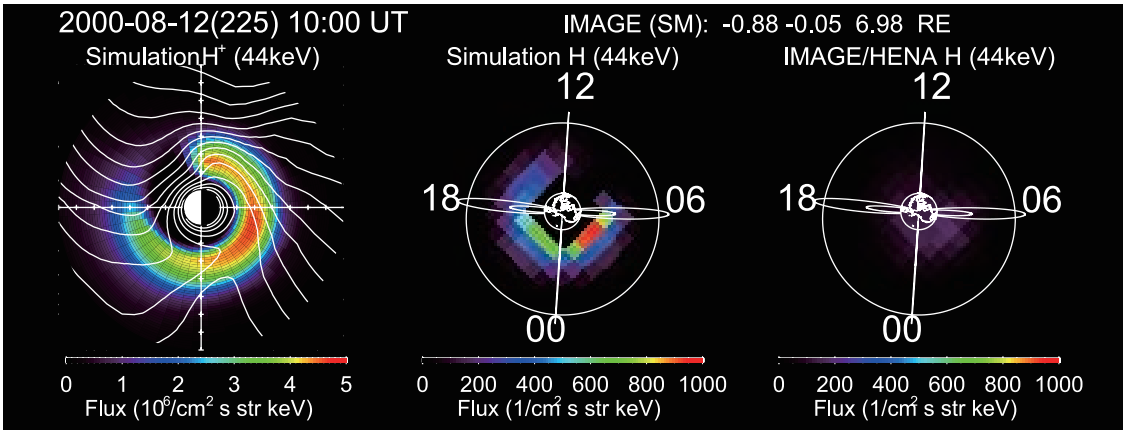

Figure 7. Comparison between the prediction of the ENA image by the CRCM and the observed ENA image. (left) Simulated proton flux distribution obtained using the orginal CRCM. (middle) ENA image derived from the proton distribution simulated by the original CRCM in the left panel. (right) ENA image observed by IMAGE/HENA at 1000 UT on 12 August 2000. The original CRCM clearly overestimates observed ENA flux.

eastward edge of the ring current region, proton flux in other region is determined with rather small uncertainty.

[14] The contours of electric potential including the corotation electric field are also shown in Figure 3 with white lines. The contour interval is 10 kV. The general features of the potential pattern in the assimilation results are similar to those in the reference model. It is notable that a distorted structure in the potential pattern and a westward electric field around the dawn are well reproduced in the assimilation results, but not in the Volland-Stern model. This westward electric field has been suggested to be one of the probable causes of the postmidnight enhancement of ENA emission [*Ebihara and Fok*, 2004]. The assimilation of ENA data is effective to improve the reproduction of the westward electric field, to which the ENA flux is sensitive. The westward electric field enhances ENA emission by energizing ions due to conservation of the first two adiabatic invariants and transporting the ions toward the geocoronal region nearer the Earth.

[15] Beyond $6R_E$, where ENA emission becomes weak, the electric potential pattern given by data assimilation is more similar to the Volland-Stern model than to the reference simulation, especially on the duskside. Actually, the uncertainty of the electric potential around the dusk was about two times larger than other local time. This indicates that the electric potential structure beyond $6R_E$ on the duskside was little effect on the ENA images observed by the IMAGE satellite. The parts of the electric fields that have a small influence on the ENA flux tend to be estimated by the Volland-Stern model that forms the base of the method. The model of the electric field in the entire inner magnetosphere could be further improved by including other data sets as constraints. For example, the use of in situ particle data could be used for improving the electric potential distribution as done by *McIlwain* [1986] and *Kistler et al.* [1989]. More accurate results could also be obtained by employing a more realistic model than the Volland-Stern model. For example, in practical cases that real data are assimilated into the model, the assimilation might provide better estimates by starting with an electric field distribution derived using the CRCM with the RCM, which was used in the present study to generate the artificial data.

[16] Figure 5 compares the proton density at the outer boundary of the simulation domain between the estimate using data assimilation (solid line) and the prediction derived from the equation of *Ebihara and Ejiri* [2000] (dotted line), which was used in the reference simulation for generation of the artificial data. Data assimilation successfully estimated the proton density at the outer boundary for the period after 0700 UT. Before 0700 UT, the estimate of the outer boundary proton density rather deviates from the density variation used in the reference simulation. This would suggest that the outer boundary condition before 0700 UT make little effects on the ENA observation after 0900 UT and that it takes about 2 h for protons to convect from $10R_E$ to the geocoronal region.

[17] The present data assimilation scheme provides a dynamic solution of the ring current variation. The left side of Figure 6 indicates the snapshots of the ring current proton distribution extracted from the dynamic solution for every hour from 0900 UT to 1200 UT. The ring current proton distribution obtained from the CRCM with the RCM, which generated the artificial data set, and the corresponding ENA flux are also shown in the right side of this figure for reference. Data assimilation appropriately reproduced the variation of the ring current ion flux.

[18] The proposed technique is designed to be robust to noises in the observed ENA data. As the kinetic ring current model is fitted to the ENA observations, the simulation model constrains the estimation so as to satisfy spatial and temporal continuity, which ensures the robustness of the estimation. As described above, the artificial ENA count data are assumed to obey a Poisson distribution in order to consider Poisson noises superimposed on the ENA data. To check the robustness to such Poisson noises, several data assimilation experiments are performed using artificial data with different seeds of random numbers (i.e., different Poisson noises). It was confirmed through these experiments that the change in the electric potential due to the

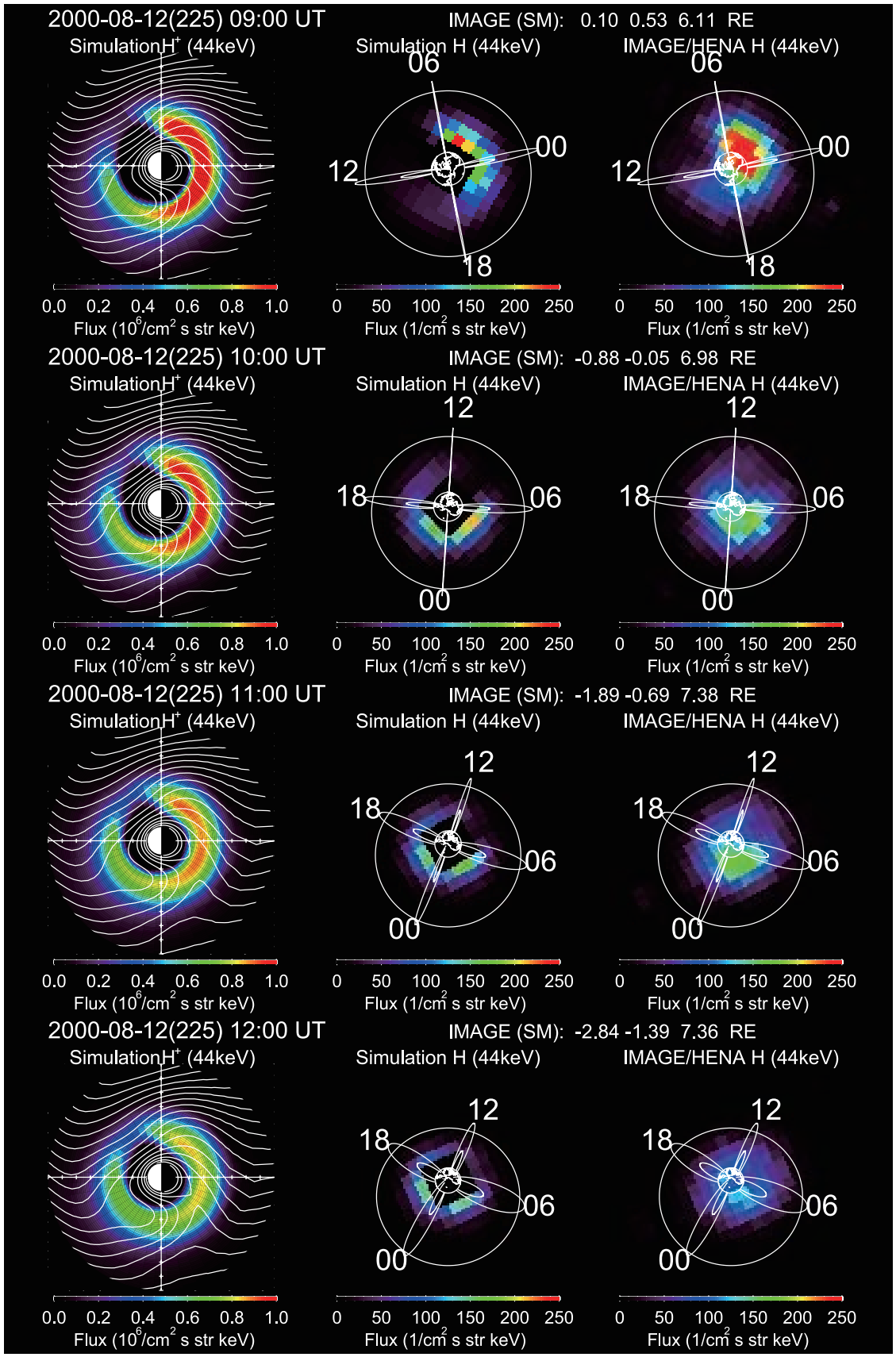

Figure 8. (left) Proton flux distribution obtained by data assimilation of real data for every hour from 0900 UT to 1200 UT. (middle) ENA images derived from the result of data assimilation. (right) ENA images observed by IMAGE/HENA. Note that the color scale is different from that in Figures 6 and 7.

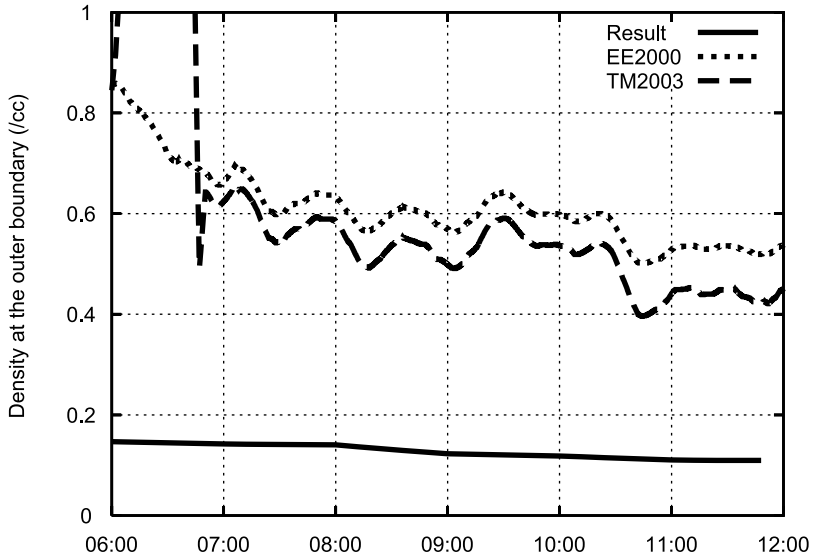

Figure 9. The proton density at the outer boundary of the simulation domain estimated using data assimilation of real data (solid line), plasma sheet ion density given by the equation of *Ebihara and Ejiri* [2000] (dotted line), and plasma sheet ion density given by the model by *Tsyganenko and Mukai* [2003] (dashed line).

noise is approximately 1% of the polar cap potential drop. The effect of noise on the ring current ion flux was found to be negligible. However, it should be noted that the assimilation results contains errors due to residuals in representing an electric field by the function of equation (2). In the case of the experiment performed in this study, the root-mean-square of the residuals in fitting the function of equation (2) to an electric field calculated by the RCM (Rice Convection Model) was approximately 5% of the polar cap potential drop. The root-mean-square of errors in ring current ion flux due to the fitting residuals were also estimated to be approximately 5% of the peak. Thus, we should think that total errors of the assimilation results is larger than errors due to observation noises.

4. An Application

[19] On the basis of the above data assimilation technique, we assimilate the real IMAGE/HENA data set into the simplified CRCM in this section. As well as the above experiment, we address the magnetic storm on 12 August 2000. Although the original CRCM, in which the electric potential is calculated with the RCM and the boundary condition is given by an empirical model, reproduces features of the ENA images observed by IMAGE/HENA for this storm in general [*Ebihara and Fok*, 2004], it tends to overestimate the ENA flux as shown in Figure 7, which compares an actual ENA image from IMAGE/HENA and an estimation of an ENA image by the original CRCM at 1000 UT on 12 August 2000. Thus, the main purpose to apply data assimilation for this storm here is to obtain a ring current model consistent with the level of ENA flux observed by IMAGE/HENA. We used 12-min averaged HENA data during the period from 0900 UT to 1200 UT when the IMAGE satellite was near the apogee altitude (see Figure 1 again), and assimilated them into the simplified version of the CRCM.

[20] Figure 8 displays the result of data assimilation of the real IMAGE/HENA data for the magnetic storm on 12 August 2000. The left panel of each row shows the ring current proton flux distribution estimated using data assimilation. For reference, in the middle panel and the right panel of each row, the ENA image derived from each data assimilation result and the observed ENA image are respectively shown. The result shows that the ring current proton flux was about a fifth of the estimates from the original CRCM shown in the right side of Figure 6. (Note that the color scale in Figure 8 is different from that in Figure 6.) Besides the intensity level, general features of the spatial distribution of ring current protons are consistent with the original CRCM. The ring current intensity is higher on the nightside than on the dayside. On the dayside, the ring current is stronger in the afternoon than in the morning. This feature of spatial distribution of the ring current is also consistent with other statistical analysis of in situ magnetic observations [e.g., *Iijima et al.*, 1990; *Terada et al.*, 1998; *Le et al.*, 2004] and in situ plasma observations [e.g., *De Michelis et al.*, 1997, 1999].

[21] The white lines in each panel of Figure 8 indicate the contours of estimated electric potential including the corotation electric field as well as in Figures 3 and 6. Again the contour interval is 10 kV. The general features of the potential pattern are similar to those in the result from the original CRCM. As well as in the original CRCM, a westward electric field appears around the dawn. This result is deduced apart from the RCM, and it would offer an evidence supporting the result of the original CRCM which used the RCM for considering self-consistency of the electric field and the electric current in both the magnetosphere and the ionosphere from another perspective. *Kistler et al.* [1989] suggests that the ion energy spectrum observed on the dayside could be explained a Volland-Stern type field with a rotation by 2 h local time. Their result can be interpreted to indicate that positions of the entry and the

drainage of ions into the ring current region are not located symmetrically about the dawn-dusk meridian but that these positions are skewed eastward. Figure 8 suggests that the contours of the electric field on the nightside are skewed eastward as approaching from the tail toward the Earth as suggested by *Brandt et al.* [2002b], and thus ions are mainly fed into the ring current region around the postmidnight. This figure also suggests a westward electric field in the afternoon sector, which corresponds to the drainage of ring current ions. Therefore, the result of the present data assimilation would be related with the result by *Kistler et al.* [1989].

[22] Figure 9 shows the proton density at the outer boundary estimated using data assimilation with a solid line. Plasma sheet ion density given by the equation of *Ebihara and Ejiri* [2000] and that given by the model by *Tsyganenko and Mukai* [2003] are also indicated with a dotted line and a dashed line, respectively, for reference. The estimated proton density is much lower than the empirical models. In the original simulation shown in the right side of Figures 6 and 7, the proton density at the outer boundary was given by the equation of *Ebihara and Ejiri* [2000]. Therefore, the overestimation of the ENA flux in the original model would be attributed to the overestimation of the amount of protons fed from the outer boundary. The large discrepancy between the estimate of data assimilation and the empirical models is acceptable. Various observations suggests that the ring current is dominated by oxygen ions during strong magnetic storms [e.g., *Daglis*, 1997]. Thus it is probable that the plasma sheet plasma contains a high percentage of oxygen ions. If oxygen ions dominate the plasma sheet plasma, it would not be valid to estimate the amount of plasma sheet protons by a model of plasma sheet ions which does not distinguish among different ion species, and thus the amount of plasma sheet protons should be overestimated. Otherwise, even if the model by *Tsyganenko and Mukai* [2003] predicts that plasma sheet ion density is about 0.5/cc, actual ion density is often below 0.2/cc (see Figure 6 in the paper by *Tsyganenko and Mukai* [2003]). Therefore an empirical model may sometimes overestimate the amount of plasma sheet protons. Anyhow, since it is basically difficult to predict the plasma sheet proton density by using an empirical model for each event, it would be meaningful to improve a guess about plasma sheet proton density by using data assimilation.

5. Summary

[23] A data assimilation method that combines IMAGE/HENA data with a simplified version of the comprehensive ring current model (CRCM) was proposed. Data assimilation is an approach which combines a physics-based model and observations to produce optimal estimates of states of a time-varying system. In this method, the magnetospheric electric potential distribution is represented by the sum of the Volland-Stern type field and a deviation from it, and the deviation is estimated simultaneously with the ring current ion distribution so as to be consistent with the ENA observations from the IMAGE satellite. The data assimilation is performed using the particle filter (PF) algorithm which allows us to treat high-dimensional systems and observations with relatively low computational cost. The method was tested using artificial data generated by the original CRCM in which the electric potential is calculated with the Rice convection model (RCM). It was demonstrated that the assimilation method can successfully reproduces the ring current ion distribution in the inner magnetosphere. The features of the electric field structures in the original CRCM are also well reconstructed including the distortion in the electric potential pattern and a westward electric field around the dawn which would cause the postmidnight enhancement of ENA emission. Although the estimation was less accurate for the region with weaker ENA emission, the accuracy in this region could be improved by incorporating other data sets and by starting with a more realistic model than the Volland-Stern model. An example of data assimilation of real ENA data from IMAGE/HENA into the ring current model was also illustrated, and the usefulness of the present data assimilation technique has been shown. Although averaged features of the ring current distribution have been examined in many literatures [e.g., *Terada et al.*, 1998; *De Michelis et al.*, 1999; *Le et al.*, 2004], it was difficult to resolve the temporal variations of the ring current distribution for each magnetic storm with in-situ measurements. The data assimilation of the global ENA observation offers the possibility to investigate time-varying spatial structures of the ring current and to resolve differences among various magnetic storms when ENA observation is available. Moreover, the features of the electric field distribution which affect the ring current structures could be also investigated for various magnetic storms.

Appendix A: Method of Assimilation

[24] The PF is a useful algorithm that is applicable to general nonlinear problems, and which can be readily implemented (see *Kitagawa and Gersch* [1996] and *Higuchi and Kitagawa* [2000] for details). The general algorithm of the PF is described briefly in subsection A1. In subsections A2 and A3, supplementary information relating to the effective application of the PF to the ring current model is provided.

A1. Particle Filter

[25] The following state-space model is considered:

$$\boldsymbol{x}_k = F_k(\boldsymbol{x}_{k-1}) + \boldsymbol{v}_k \tag{A1a}$$

$$\boldsymbol{y}_k = H_k(\boldsymbol{x}_k) + \boldsymbol{w}_k \tag{A1b}$$

where the vectors $\boldsymbol{x}_k$ and $\boldsymbol{y}_k$ indicate the state of a system and the observed data at the discrete time $T = t_k$, and the vectors $\boldsymbol{v}_k$ and $\boldsymbol{w}_k$ denote system noise and observation noise. The state vector $\boldsymbol{x}_k$ consists of the target variables in the simulation model. In the present study, $\boldsymbol{x}_k$ is composed of discretized phase-space densities of ring current ions and the coefficient a_{ij} and b_{ij} in equation (2). The observation vector $\boldsymbol{y}_k$ corresponds to the differential ENA flux data for each pixel of the HENA image. The operator F_k represents the temporal evolution from time t_{k-1} to time t_k according to the simulation, while H_k projects the state vector $\boldsymbol{x}_k$ to the observation space. In this study, H_k relates the observed

ENA flux to the proton phase-space density in the simulation model. The structure of H_k is described in detail in subsection A3.

[26] In the PF as well as the ensemble Kalman filter, the probability distribution of the state $\boldsymbol{x}_k$ is considered. The probability distribution is approximated by an ensemble consisting of a large number of realizations called "particles." First, the probability distribution of the initial state of a system $p(\boldsymbol{x}_0)$ is approximated by particles $\{\boldsymbol{x}_0^{(1)}, \boldsymbol{x}_0^{(2)}, \cdots, \boldsymbol{x}_0^{(n)}\}$ such that

$$p(\boldsymbol{x}_0) \approx \sum_{i=1}^{n} w_0^{(i)} \delta\left(\boldsymbol{x}_0 - \boldsymbol{x}_0^{(i)}\right) \tag{A2}$$

where δ is Dirac's delta function and n is the number of particles. The initial weight $w_0^{(i)}$ is set at $1/n$ for all i. On the basis of the particle approximation, the probability distribution of the state at the first observation time t_1, $p(\boldsymbol{x}_1)$, is derived from $p(\boldsymbol{x}_0)$ (prediction step). The probability distribution $p(\boldsymbol{x}_1)$ is referred to as a predictive distribution. By incorporating the information of the observation $\boldsymbol{y}_1$ into the predictive distribution $p(\boldsymbol{x}_1)$, the posterior probability distribution $p(\boldsymbol{x}_1|\boldsymbol{y}_1)$ is derived (filtering step). From the filtered distribution $p(\boldsymbol{x}_1|\boldsymbol{y}_1)$, the predictive distribution at the next observation time t_2, $p(\boldsymbol{x}_2|\boldsymbol{y}_1)$ is deduced, and the next observation $\boldsymbol{y}_2$ is used for the constraint to obtain the filtered distribution $p(\boldsymbol{x}_2|\boldsymbol{y}_1, \boldsymbol{y}_2)$ from $p(\boldsymbol{x}_2|\boldsymbol{y}_1)$. By applying the prediction and filtering steps recursively, the filtered distribution $p(\boldsymbol{x}_k|\boldsymbol{y}_1, \cdots, \boldsymbol{y}_k)$ is obtained for any observation time t_k. The implementation of the prediction step and the filtering step is as follows.

[27] Suppose that a filtered distribution of the state at time $T = t_{k-1}$ has been obtained given the data at times $T = t_1, \cdots, t_{k-1}$ in the form of the particle approximation as

$$p(\boldsymbol{x}_{k-1}|\boldsymbol{y}_{1:k-1}) \approx \sum_{i=1}^{n} w_{k-1}^{(i)} \delta\left(\boldsymbol{x}_{k-1} - \boldsymbol{x}_{k-1}^{(i)}\right) \tag{A3}$$

where $p(\boldsymbol{x}_{k-1}|\boldsymbol{y}_1, \cdots, \boldsymbol{y}_{k-1})$ is expressed as $p(\boldsymbol{x}_{k-1}|\boldsymbol{y}_{1:k-1})$. The weight $w_{k-1}^{(i)}$ for each particle is set to satisfy $\sum_i w_{k-1}^{(i)} = 1$. From $p(\boldsymbol{x}_{k-1}|\boldsymbol{y}_{1:k-1})$, a predictive distribution of the state at the next observation time t_k is obtained by

$$p(\boldsymbol{x}_k|\boldsymbol{y}_{1:k-1}) \approx \sum_{i=1}^{n} w_{k-1}^{(i)} \delta\left(\boldsymbol{x}_k - \boldsymbol{x}_k^{(i)}\right) \tag{A4}$$

where $\boldsymbol{x}_k^{(i)}$ is given by $F_k(\boldsymbol{x}_{k-1}^{(i)}) + \boldsymbol{v}_k^{(i)}$ for each i and $F_k(\boldsymbol{x}_{k-1}^{(i)})$ is obtained by advancing the simulation from the state $\boldsymbol{x}_{k-1}^{(i)}$. Using the predictive distribution $p(\boldsymbol{x}_k|\boldsymbol{y}_{1:k-1})$ as a prior distribution, the posterior filtered distribution $p(\boldsymbol{x}_k|\boldsymbol{y}_{1:k})$ $(= p(\boldsymbol{x}_k|\boldsymbol{y}_1, \cdots, \boldsymbol{y}_{k-1}, \boldsymbol{y}_k))$ is obtained using the data at time $T = t_k$, $\boldsymbol{y}_k$. The particle approximation of the filtered distribution is calculated using Bayes' theorem as follows.

$$\begin{aligned} p(\boldsymbol{x}_k|\boldsymbol{y}_{1:k}) &= \frac{p(\boldsymbol{x}_k|\boldsymbol{y}_{1:k-1}) p(\boldsymbol{y}_k|\boldsymbol{x}_k)}{\int p(\boldsymbol{x}_k|\boldsymbol{y}_{1:k-1}) p(\boldsymbol{y}_k|\boldsymbol{x}_k) d\boldsymbol{x}_k} \\ &\approx \frac{1}{\sum_j w_{k-1}^{(j)} p\left(\boldsymbol{y}_k|\boldsymbol{x}_k^{(j)}\right)} \sum_{i=1}^{n} p\left(\boldsymbol{y}_k|\boldsymbol{x}_k^{(i)}\right) \cdot w_{k-1}^{(i)} \cdot \delta\left(\boldsymbol{x}_k - \boldsymbol{x}_k^{(i)}\right). \end{aligned} \tag{A5}$$

Here, $p(\boldsymbol{y}_k|\boldsymbol{x}_k^{(i)})$ is the likelihood of $\boldsymbol{x}_k^{(i)}$ given data $\boldsymbol{y}_k$, and is obtained as described in section A3. The weight is then updated by

$$w_k^{(i)} = \frac{w_{k-1}^{(i)} \cdot p\left(\boldsymbol{y}_k|\boldsymbol{x}_k^{(i)}\right)}{\sum_j w_{k-1}^{(j)} \cdot p\left(\boldsymbol{y}_k|\boldsymbol{x}_k^{(j)}\right)} \tag{A6}$$

for each i, and equation (A5) is rewritten as

$$p(\boldsymbol{x}_k|\boldsymbol{y}_{1:k}) \approx \sum_{i=1}^{n} w_k^{(i)} \delta\left(\boldsymbol{x}_k - \boldsymbol{x}_k^{(i)}\right). \tag{A7}$$

[28] This is the same form as equation (A3). In the PF, a procedure called "resampling" is usually performed as an alternative to the weight updating as described in equation (A6). The resampling procedure corresponds to a sort of approximation of equation (A5) (see *Kitagawa and Gersch* [1996] and *Higuchi and Kitagawa* [2000]) but is not implemented in this study.

[29] Finally, constraints are imposed on the state in the past by pursuing the history of each particle contained in the ensemble $\boldsymbol{x}_k^{(1)}, \cdots, \boldsymbol{x}_k^{(n)}$. The procedure to constrain the state in the past is called "particle smoother." As the previous state $\boldsymbol{x}_{k-1}^{(i)}$ for each particle in the ensemble is known, the distribution of $\boldsymbol{x}_{k-1}$ given the data sequence $\{\boldsymbol{y}_1, \cdots, \boldsymbol{y}_k\}$ (smoothed distribution) is obtained by

$$p(\boldsymbol{x}_{k-1}|\boldsymbol{y}_{1:k}) \approx \sum_{i=1}^{n} w_k^{(i)} \delta\left(\boldsymbol{x}_{k-1} - \boldsymbol{x}_{k-1}^{(i)}\right). \tag{A8}$$

After the filtered distributions have been obtained to the end of the data sequence, the smoothed distribution $p(\boldsymbol{x}_k|\boldsymbol{y}_{1:\mathrm{end}})$, that is, the posterior distribution of $\boldsymbol{x}_k$ given all of the data sequence, is obtained for all k. The smoothed distribution at each observation time provides an optimal estimate of the state.

A2. Notes for Application

[30] As mentioned above, the state vector $\boldsymbol{x}_k$ consists of discretized phase-space densities of ring current ions and the coefficients a_{ij} and b_{ij} in equation (2). Thus, the vector $\boldsymbol{x}_k$ is divided into two parts as follows.

$$\boldsymbol{x}_k = \begin{pmatrix} \boldsymbol{f}_k \\ \boldsymbol{u} \end{pmatrix} (= \boldsymbol{f}_k + \boldsymbol{u}). \tag{A9}$$

Here, $\boldsymbol{f}_k$ is the discretized phase-space density and $\boldsymbol{u}$ is a vector consisting of a_{ij} and b_{ij} for all i and j and a time sequence of the ion density at the outer boundary. We can treat $\boldsymbol{u}$ as a time constant.

[31] As the dimension of $\boldsymbol{f}_k$ in $\boldsymbol{x}_k$ is larger than 2,000,000, the dimension of $\boldsymbol{x}_k$ is extremely large. It is practically impossible to deal with uncertainties for a vector of such a size by the PF. Uncertainties are therefore only imposed on $\boldsymbol{u}$, that is, only on the coefficients a_{ij} and b_{ij}, and the sequence of the parameter of the outer boundary condition. Then, the values of these uncertain parameters are improved in the course of the data assimilation. The initial guess of a_{ij} and b_{ij} are set to be zero, and the uncertainties of them are

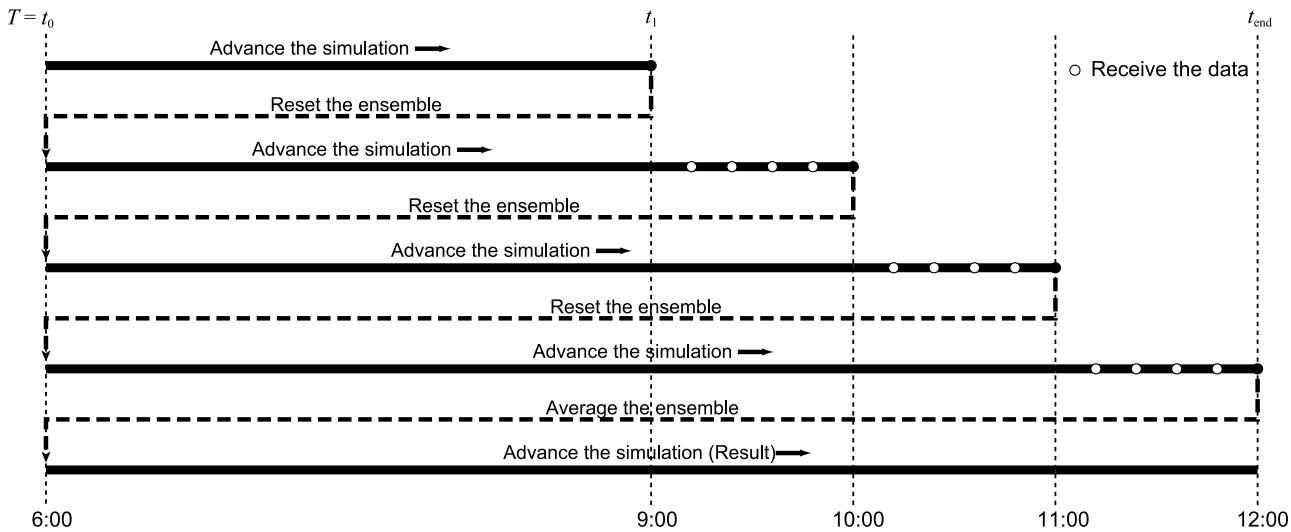

Figure A1. Assimilation scheme. ENA data are referred to every 12 min. Open circles denote times of referral to observed data and update of weights, solid circles denote times at which the probability distribution of $\vec{x}_0$ is reset by updating the ensemble on the basis of comparison with observed data.

assumed to obey Gaussian distributions with certain standard deviations. The initial values of the phase-space density $\boldsymbol{f}_0$ are given by the proton fluxes measured by AMPTE/CCE with no uncertainties, as is the case for the run to generate the artificial data. The model for the assimilation is initialized at 0600 UT to allow 3 h for the ion distribution to reach equilibrium, while the simulation run to generate the artificial data is started at 0200 UT. System noise $\boldsymbol{v}_k$ in equation (A1a) is also neglected. The dynamical system therefore becomes

$$\boldsymbol{x}_k = F(\boldsymbol{x}_{k-1}). \tag{A10}$$

The simulation model is thus assumed to correctly represent the dynamics of the ring current. The assumption that uncertainties are entirely due to $\boldsymbol{u}$ reduces the dimension of the uncertainties considerably, making it possible to represent the uncertainties by a limited number of particles. The number of particles n was set at 512 in this study.

[32] A problem that often occurs in the PF is particle degeneration. In the PF, as the filtering procedure is applied recursively, the approximation of the filtered distribution is dominated by only one or two particles of the ensemble, with the contribution from other particles becoming negligible. This may spoil the validity of the particle approximation of the probability distribution. Although this problem can be avoided by increasing the number of particles in the ensemble, doing so increases the computational cost and resource requirements. To avoid particle degeneration with less computational cost, the ensemble is reset every hour of simulation time, as described below.

[33] First, with the weights calculated by equation (A6), a particle approximation of the smoothed distribution $p(\boldsymbol{x}_0|\boldsymbol{y}_{1:k})$ is obtained as equation (A8). From the smoothed distribution, the posterior probability distribution of $\boldsymbol{u}$ is approximated by

$$p(\boldsymbol{u}|\boldsymbol{y}_{1:k}) \approx \sum_{i=1}^{n} w_k^{(i)} \delta\left(\boldsymbol{u} - \boldsymbol{u}^{(i)}\right) \tag{A11}$$

where $\boldsymbol{u}^{(i)} = \boldsymbol{x}_0^{(i)} - \boldsymbol{f}_0$. The sample mean and covariance of $\boldsymbol{u}$ are given by

$$\boldsymbol{\mu}_{1:k} = \sum_{i=1}^{n} w_k^{(i)} \boldsymbol{u}^{(i)} \tag{A12a}$$

$$\Sigma_{1:k} = \sum_{i=1}^{n} w_k^{(i)} \left(\boldsymbol{u}^{(i)} - \boldsymbol{\mu}_{1:k}\right)\left(\boldsymbol{u}^{(i)} - \boldsymbol{\mu}_{1:k}\right)^T. \tag{A12b}$$

Suppose that $p(\boldsymbol{u}|\boldsymbol{y}_{1:k})$ follows a Gaussian distribution with mean $\boldsymbol{\mu}_{1:k}$ and covariance $\boldsymbol{\Sigma}_{1:k}$. A new approximation of $p(\boldsymbol{u}|\boldsymbol{y}_{1:k})$ can then be obtained by drawing samples $\{\boldsymbol{u}_{1:k}^{(1)}, \cdots, \boldsymbol{u}_{1:k}^{(n)}\}$ from the Gaussian as

$$p(\boldsymbol{u}|\boldsymbol{y}_{1:k}) \approx \sum_{i=1}^{n} w_{0|1:k}^{(i)} \delta\left(\boldsymbol{u} - \boldsymbol{u}_{1:k}^{(i)}\right) \tag{A13}$$

where $w_{0|1:k}^{(i)}$ is set as $1/n$ for all i. Deriving $\boldsymbol{x}_{0|1:k}^{(i)}$ from $\boldsymbol{u}_{1:k}^{(i)}$ by adding $\boldsymbol{f}_0$ for each i, the particle approximation of $p(\boldsymbol{x}_0|\boldsymbol{y}_{1:k})$ is reconstructed, and the approximation of the filtered distribution $p(\boldsymbol{x}_k|\boldsymbol{y}_{1:k})$ is obtained as

$$p(\boldsymbol{x}_k|\boldsymbol{y}_{1:k}) \approx \sum_{i=1}^{n} w_{k|1:k}^{(i)} \delta\left(\boldsymbol{x}_k - \boldsymbol{x}_{k|1:k}^{(i)}\right) \tag{A14}$$

with the updated ensemble $\{\boldsymbol{x}_{k|1:k}^{(1)}, \cdots, \boldsymbol{x}_{k|1:k}^{(n)}\}$. Here, $\boldsymbol{x}_{k|1:k}^{(i)}$ is given by applying the operator F to $\boldsymbol{x}_{0|1:k}^{(i)}$ recursively, that is, $\boldsymbol{x}_{k|1:k}^{(i)}$ is the result of the simulation started with the initial state of $\boldsymbol{x}_{0|1:k}^{(i)}$.

[34] The assimilation process is illustrated in Figure A1. The model for the assimilation is started at time $T = t_0$, which corresponds to 0600 UT in the present case. The open circles denote the times at which referral is made to the observed data and weights are updated by equation (A6), while the solid circles denote the times at which the ensemble is reset and the filtered distribution $p(\boldsymbol{x}_k|\boldsymbol{y}_{1:k})$ is approximated by equation (A14). Every hour of simulation

time from $T = t_1$ (0900 UT), the data are referred to five times, among which the weights are updated four times and the ensemble is updated once. After referring to the data at $T = t_{\mathrm{end}}$ (1200 UT) and updating the weights $\{w_{\mathrm{end}}^{(1)}, \cdots, w_{\mathrm{end}}^{(n)}\}$, the mean of $\boldsymbol{u}$, $\boldsymbol{\mu}_{1:\mathrm{end}}$ is calculated by equation (A12a). The optimal initial state is then obtained as $\boldsymbol{f}_0 + \boldsymbol{\mu}_{1:\mathrm{end}}$, which is the mean of the smoothed distribution of the initial state $p(\boldsymbol{x}_0|\boldsymbol{y}_{1:\mathrm{end}})$. Finally, the simulation is advanced from the optimal initial state $\boldsymbol{f}_0 + \boldsymbol{\mu}_{1:\mathrm{end}}$, and the result of the simulation run is adopted as the result of the assimilation, as shown in the middle panels of Figures 2 and 3.

A3. Calculation of Likelihood Function

[35] As described in subsection A1, the PF algorithm requires the likelihood of $\boldsymbol{x}_k^{(i)}$ given the data $\boldsymbol{y}_k$, $p(\boldsymbol{y}_k|\boldsymbol{x}_k^{(i)})$. Since the likelihood has a significant effect on the results of assimilation, the algorithm for calculating the likelihood is important. The likelihood function is calculated here considering the relationship between $\boldsymbol{y}_k$ and $\boldsymbol{x}_k$ given by equation (A1b) as follows.

[36] The operator H_k in equation (A1b) includes the relationship between ENA flux data and the proton differential flux given by equation (3), and the conversion from phase-space density to differential flux. On the basis of a discrete approximation of the line-of-sight integral in equation (3), the relationship between an ENA flux datum for each pixel $J_{\mathrm{ENA},k}^p$ and the equatorial proton differential flux at each l_{is}-ϕ_{is} grid $\bar{J}_{\mathrm{proton},\,k}^q$ can be modeled as

$$J_{\mathrm{ENA},k}^p = \sum_q C_{pq,k}\left(\bar{J}_{\mathrm{proton},k}^q + \delta_k^q\right) \tag{A15}$$

where δ_k^q is noise superposed on $\bar{J}_{\mathrm{proton},k}^q$. The noise δ_k^q includes uncertainty in representing the ring current ion density by the ring current model, uncertainty in the neutral density model, and fluctuation in the charge exchange process. The uncertainty in representing the ion density by the model is regarded as the dominant contribution to δ_k^q, since the main focus of this approach is to improve the poor reproduction of ion density based on a poor electric field model (the Volland-Stern model). The coefficient $C_{pq,k}$ contains information on the efficiency of ENA generation by charge exchange between ring current protons and neutrals, and the geometric configuration and the line-of-sight integral of ENA flux. The coefficient is derived using the neutral density model and the magnetospheric magnetic field model described in section 2. Equation (A15) is expressed in vector form as

$$\boldsymbol{J}_{\mathrm{ENA},k} = C_k\left(\bar{\boldsymbol{J}}_{\mathrm{proton},k} + \boldsymbol{\delta}_k\right). \tag{A16}$$

The function ϕ is introduced to convert the state vector $\boldsymbol{x}_k$ into $\bar{\boldsymbol{J}}_{\mathrm{proton},k}$, that is, $\bar{\boldsymbol{J}}_{\mathrm{proton},k} = \boldsymbol{\phi}(\boldsymbol{x}_k)$. Equation (A16) then becomes

$$\boldsymbol{y}_k = C_k[\boldsymbol{\phi}(\boldsymbol{x}_k) + \boldsymbol{\delta}_k] \tag{A17}$$

where $\boldsymbol{J}_{\mathrm{ENA},k}$ is replaced by $\boldsymbol{y}_k$ according to the notation used in equation (A1b). The relationship between $\boldsymbol{x}_k$ and $\bar{\boldsymbol{J}}_{\mathrm{proton},k}$ is described as nonlinear because the discretized phase-space densities $\boldsymbol{f}_k$ in $\boldsymbol{x}_k$ are converted into discretized differential fluxes by interpolation on a logarithmic scale. According to the notation of equation (A1b), the operator $C_k\phi()$ denotes $H()$. Thus, equation (A17) can be rewritten as

$$\boldsymbol{y}_k = H_k(\boldsymbol{x}_k) + C_k\boldsymbol{\delta}_k. \tag{A18}$$

The vector $\boldsymbol{\delta}_k$ is assumed to follow a Gaussian distribution, and $\boldsymbol{\delta}_k$ is assumed to satisfy $E(\boldsymbol{\delta}_k) = 0$ and $E(\boldsymbol{\delta}_k\boldsymbol{\delta}_k^T) = \eta^2 I$. Since δ_k^q is dominated by uncertainty in representing the state by the model, η is determined by the uncertainty in proton flux. If $\boldsymbol{x}_k$ is given, $\boldsymbol{y}_k$ also follows a Gaussian distribution, having a mean of $H_k(\boldsymbol{x}_k)$. The covariance matrix of $\boldsymbol{y}^k$ given $\boldsymbol{x}_k$ thus becomes

$$\begin{aligned} R_k &= E\Big((\boldsymbol{y}_k - H_k(\boldsymbol{x}_k))(\boldsymbol{y}_k - H_k(\boldsymbol{x}_k))^T|\boldsymbol{x}_k\Big) \\ &= E\big(C_k\boldsymbol{\delta}_k\boldsymbol{\delta}_k^T C_k^T\big) = \eta^2 C_k C_k^T. \end{aligned} \tag{A19}$$

The likelihood is therefore given by

$$p(\boldsymbol{y}_k|\boldsymbol{x}_k) = \frac{1}{\sqrt{(2\pi)^m|R_k|}}\exp\left[-\frac{(\boldsymbol{y}_k - H_k(\boldsymbol{x}_k))^T R_k^{-1}(\boldsymbol{y}_k - H_k(\boldsymbol{x}_k))}{2}\right] \tag{A20}$$

where m denotes the dimension of the vector $\boldsymbol{y}_k$. Substituting $\boldsymbol{x}_{k|k-1}^{(i)}$ for $\boldsymbol{x}_k$ in equation (A20) leads to $p(\boldsymbol{y}_k|\boldsymbol{x}_{k|k-1}^{(i)})$.

[37] **Acknowledgments.** This study was supported by the Japan Science and Technology Agency (JST) under the Core Research for Evolutional Science and Technology (CREST) program and in part by Transdisciplinary Research Integration Center, Research Organization of Information and Systems (ROIS/TRIC) as a Function and Induction Research Project. Work at the Johns Hopkins University Applied Physics Laboratory (JHUAPL) was supported by the National Science Foundation (NSF; grant ATM0318173) and the National Aeronautics and Space Administration (NASA; grant NAG513491). Some of the numerical calculations were performed on a super computer of the Computing and Communications Center, National Institute of Polar Research. The authors thank the ACE Magnetic Field Instrument team (PI N. Ness) and the ACE Science Center for providing the ACE data. The D_{st} index was provided by the World Data Center for Geomagnetism, Kyoto University.

[38] Zuyin Pu thanks the reviewers for their assistance in evaluating this paper.

References

Brandt, P. C., R. Demajistre, E. C. Roelof, S. Ohtani, D. G. Mitchell, and S. Mende (2002a), IMAGE/high-energy energetic neutral atom: Global energetic neutral atom imaging of the plasma sheet and ring current during substorms, *J. Geophys. Res.*, *107*(A12), 1454, doi:10.1029/2002JA009307.

Brandt, P. C., S. Ohtani, D. G. Mitchell, M.-C. Fok, E. C. Roelof, and R. Demajistre (2002b), Global ENA observations of the storm main-phase ring current: Implications for skewed electric fields in the inner magnetosphere, *Geophys. Res. Lett.*, *29*(20), 1954, doi:10.1029/2002GL015160.

Chen, M. W., M. Schulz, L. R. Lyons, and D. J. Gorney (1993), Storm-time transport of ring current and radiation belt ions, *J. Geophys. Res.*, *98*, 3835.

Daglis, I. A. (1997), The role of magnetosphere-ionosphere coupling in magnetic storm dynamics, in *Magnetic Storms*, *Geophys. Monogr. Ser.*, 98, edited by B. T. Tsurutani et al., p. 107, AGU, Washington, D. C.

DeMajistre, R., E. C. Roelof, P. C. Brandt, and D. G. Mitchell (2004), Retrieval of global magnetospheric ion distributions from high-energy neutral atom measurements made by IMAGE/HENA instrument, *J. Geophys. Res.*, *109*, A04214, doi:10.1029/2003JA010322.

De Michelis, P., I. A. Daglis, and G. Consolini (1997), Average terrestrial ring current derived from AMPTE/CCE-CHEM measurements, *J. Geophys. Res.*, *102*, 14103.

De Michelis, P., I. A. Daglis, and G. Consolini (1999), An average image of proton plasma pressure and of current systems in the equatorial plane derived from AMPTE/CCE-CHEM measurements, *J. Geophys. Res.*, *104*, 28,615.

Ebihara, Y., and M. Ejiri (2000), Simulation study on fundamental properties of the storm-time ring current, *J. Geophys. Res.*, *105*, 15,843.

Ebihara, Y., and M.-C. Fok (2004), Postmidnight storm-time enhancement of tens-of-keV proton flux, *J. Geophys. Res.*, *109*, A12209, doi:10.1029/2004JA010523.

Evensen, G. (1992), Using the extended Kalman filter with a multilayer quasi-geostrophic model, *J. Geophys. Res.*, *97*, 17,905.

Fok, M.-C., T. E. Moore, J. U. Kozyra, G. C. Ho, and D. C. Hamilton (1995), Three-dimensional ring current decay model, *J. Geophys. Res.*, *100*, 9619.

Fok, M.-C., R. A. Wolf, R. W. Spiro, and T. E. Moore (2001), Comprehensive computational model of Earth's ring current, *J. Geophys. Res.*, *104*, 14,557.

Fok, M.-C., et al. (2003), Global ENA image simulations, *Space Sci. Rev.*, *109*, 77.

Garner, T. W., R. A. Wolf, R. W. Spiro, and M. F. Thomsen (1999), First attempt at assimilating data to constrain a magnetospheric model, *J. Geophys. Res.*, *104*, 25,145.

Gordon, N. J., D. J. Salmond, and A. F. M. Smith (1993), Novel approach to nonlinear/non-Gaussian Bayesian state estimation, *IEE Conf. Publ.*, *140*, 107.

Higuchi, T., and G. Kitagawa (2000), Knowledge discovery and self-organizing state space model, *IEICE Trans. Inf. Syst.*, *E83-D*, 36.

Iijima, T., T. A. Potemra, and L. J. Zanetti (1990), Large-scale characteristics of magnetospheric equatorial currents, *J. Geophys. Res.*, *95*, 991.

Jordanova, V. K., L. M. Kistler, J. U. Kozyra, G. V. Khazanov, and A. F. Nagy (1996), Collisional losses of ring current ions, *J. Geophys. Res.*, *101*, 111.

Kistler, L. M., F. M. Ipavich, D. C. Hamilton, G. Gloeckler, B. Wilken, G. Kremser, and W. Stüdemann (1989), Energy spectra of the major ion species in the ring current during geomagnetic storms, *J. Geophys. Res.*, *94*, 3579.

Kitagawa, G. (1993), Monte Carlo filtering and smoothing method for non-Gaussian nonlinear state space model, research memo, Inst. of Stat. Math., Tokyo.

Kitagawa, G. (1996), Monte Carlo filter and smoother for non-Gaussian nonlinear state space models, *J. Comput. Graph. Stat.*, *5*, 1.

Kitagawa, G., and W. Gersch (1996), *Smoothness Priors Analysis of Time Series*, chap. 6, Springer, New York.

Le, G., C. T. Russell, and K. Takahashi (2004), Morphology of the ring current derived from magnetic field observations, *Ann. Geophys.*, *24*, 1267.

Liemohn, M. W., J. U. Kozyra, M. F. Thomsen, J. L. Roeder, G. Lu, J. E. Borovsky, and T. E. Cayton (2001), Dominant role of the asymmetric ring current in producing the stormtime *Dst**, *J. Geophys. Res.*, *106*, 10,883.

McIlwain, C. E. (1986), A Kp dependent equatorial electric field model, *Adv. Space. Res.*, *6*(3), 187.

Mitchell, D. G., et al. (2000), High energy neutral atom (HENA) imager for the IMAGE mission, *Space Sci. Rev.*, *91*, 67.

Naehr, S. M., and F. R. Toffoletto (2005), Radiation belt data assimilation with an extended Kalman filter, *Space Weather*, *3*, S06001, doi:10.1029/2004SW000121.

Perez, J. D., X.-X. Zhang, P. C. Brandt, D. G. Mitchell, J. M. Jahn, and C. J. Pollock (2004), Dynamics of ring current ions as obtained from IMAGE HENA and MENA ENA images, *J. Geophys. Res.*, *109*, A05208, doi:10.1029/2003JA010164.

Picone, J. M., A. E. Hedin, D. P. Drob, and A. C. Aikin (2002), NRLMSISE-00 empirical model of the atmosphere: Statistical comparisons and scientific issues, *J. Geophys. Res.*, *107*(A12), 1468, doi:10.1029/2002JA009430.

Rairden, R. L., L. A. Frank, and J. D. Craven (1986), Geocoronal imaging with Dynamics Explorer, *J. Geophys. Res.*, *91*, 13,613.

Sheldon, R. B., and D. C. Hamilton (1993), Ion transport and loss in the Earth's quiet ring current: 1. Data and standard model, *J. Geophys. Res.*, *98*, 13,491.

Terada, N., T. Iyemori, M. Nosé, T. Nagai, H. Matsumoto, and T. Goka (1998), Storm-time magnetic field variations observed by the ETS-VI satellite, *Earth Planets Space*, *50*, 853.

Tsyganenko, N. A. (1995), Modeling the Earth's magnetospheric magnetic field confined within a realistic magnetopause, *J. Geophys. Res.*, *100*, 5599.

Tsyganenko, N. A., and T. Mukai (2003), Tail plasma sheet models derived from Geotail particle data, *J. Geophys. Res.*, *108*(A3), 1136, doi:10.1029/2002JA009707.

Tsyganenko, N. A., and D. P. Stern (1996), A new-generation global magnetosphere field model, based on spacecraft magnetometer data, *ISTP Newsl.*, *6*(1), 21.

Vallat, C., et al. (2004), First comparisons of local ion measurements in the inner magnetosphere with energetic neutral atom magnetospheric image inversions: Cluster-CIS and IMAGE-HENA observations, *J. Geophys. Res.*, *109*, A04213, doi:10.1029/2003JA010224.

Weimer, D. R. (2001), An improved model of ionospheric electric potentials including substorm perturbations and application to the Geospace Environment Modeling November 24, 1996 event, *J. Geophys. Res.*, *106*, 407.

P. C. Brandt, D. G. Mitchell, and S. Ohtani, Johns Hopkins University Applied Physics Laboratory, 11100 Johns Hopkins Road, Laurel, MD 20723-6099, USA. (pontus.brandt@jhuapl.edu; don.mitchell@jhuapl.edu; shin.ohtani@jhuapl.edu)

Y. Ebihara, Institute for Advanced Research, Nagoya University, Furo-cho, Chikusa-ku, Nagoya 464-8601, Japan. (ebihara@stelab.nagoya-u.ac.jp)

M.-C. Fok, NASA Goddard Space Flight Center, Code 673, Greenbelt, MD 20771, USA. (mei-ching.h.fok@nasa.gov)

T. Higuchi, S. Nakano, and G. Ueno, The Institute of Statistical Mathematics, Research Organization of Information and Systems, 4-6-7 Minami-Azabu, Minato, Tokyo 106-8569, Japan. (higuchi@ism.ac.jp; shiny@ism.ac.jp; gen@ism.ac.jp)

K. Keika, Space Research Institute, Austrian Academy of Sciences, Schmiedlstrasse 6, A-8042 Graz, Austria. (kunihiro.keika@oeaw.ac.at)